Research Article

Journal of Environmental Nanotechnology

Electrochemical Properties of Titanium Dioxide-doped Zinc Oxide by the Chemical Vapor Deposition Method

Siluvai Raju Mary Jony[1*] and S. Muruganantham[2]

[1]Department of Physics, Pavendar Bharathidasan College of Arts and Science, Mathur, Pudukkottai, TN, India
[2]Department of Physics, National College, Tiruchirappalli, TN, India
Received: 19.05.2026 Accepted: 22.06.2026 Published: xx.xx.xxxx
*boscoj10antony@gmail.com

ABSTRACT

In the era of modern trends, the nature of dopants does change the behaviour of the base material. The properties of zinc oxide have changed due to the dopant; titanium dioxide is the dopant used here. The question arises as to whether the doping will change the properties of the material. For the above query, the justification is that the researchers have done the research on this previously and have come up with solutions. Here, we have done the combinational aspect. In this idea, ZnO is taken as the base material, and then TiO_2 is used as the dopant. The additive nature used here is 90% ZnO doped with 10% titanium dioxide, named A. This is followed by 80% ZnO doped with 20% titanium dioxide, named as B. Further, 70% ZnO doped with 30% titanium dioxide, named as C. The characterization techniques like XRD, PL, UV, FTIR, CV, EIS, DSC, and TGA-DTA are used for samples A, B, and C. The characterization techniques reveal that there occurs a change in the structures leading to the understanding of physical changes as well as these better give up changes in the chemical property change called the internal changes. XRD exhibits the structural change; from XRD data, Scherrer plots and Williamson-Hall plots are plotted. A linear fit is applied; the end result features a change in the graphical arrangement from negative to positive. The values obtained from the Scherrer plot and Williamson-Hall plot nearly match; this proves that the data is acceptable. The intensity is reduced due to the use of the dopant; this is exhibited by the PL graph. From the UV spectrum, it is very clear that sample C's absorption is greater than that of A; this reveals that the dopant increases the absorption of the incoming radiation. The functional groups are clearly identified from FTIR graphs. The CV analysis shows that the resistance increases when the doping level in the base material ZnO is increased. EIS reveals electrochemical changes. The property of the material has changed in a systematic manner when the level of doping is changed. The results obtained show clearly that the change in the property has occurred systematically. The futuristic scope can preferably be extended by enhancing the work by introducing tertiary doping methods or implementing electrolytic conductivity procedures.

Keywords: Titanium dioxide-doped with zinc Oxide; CVD.

1. INTRODUCTION

The base material used here is ZnO (Wurtzite structure), and the dopant used is TiO_2. ZnO is a milky white material, which is harmless, and a semiconductor material. Researchers have preferred Zinc Oxide as the base material because its applications are quite wide. The optical and electrical properties exhibited by ZnO are fabulously acceptable. We have used the co-dopant material as Titanium dioxide (TiO2); the energy band gap of ZnO is 3.37 eV, whereas that of TiO_2 is 3.2 eV. Both materials are taken in the amorphous form. The doping is done in terms of grams; 1 gram of TiO2 is doped with 9 grams of ZnO. This is exhibited here in the form of a percentage (Brust and Kiely, 2002). The presence of 70% of ZnO is 7 gm of ZnO. The combination of materials is called a composite material. The behaviour of the composite material can be studied by characterization techniques (Guenther *et al.* 1992). Hence, the characterization techniques have shown changes in its internal properties. Mainly, composite materials are preferably focused on whether they exhibit high strength under mechanical pressure exerted on them, and whether their weight shouldn't exceed certain limits or should be less (Kim *et al.* 2002). Macroscopic properties have been previously discussed; however, microscopic properties are noted for high usability. The chemical property, electrochemical property, optical property, and mass change property are taken into consideration (Li *et al.* 2006). Structural change will always bring a change in the physical and chemical properties. A wide range of band gaps is suggested for researchers to achieve excellence in scientific growth. Semiconductor materials are widely used in optoelectronic applications like LEDs and even in lasers too. Eventually, composite materials are also used for optoelectronic applications (Li *et al.* 2002). ZnO and TiO_2 are eco-friendly; moreover, their chemical stability is appreciable. ZnO exhibits properties such as ferromagnetism when it is subjected to doping with transition metals at room temperature; in the case of spintronic applications, these features are adopted. A, B, and C are the three samples that are characterized (Li *et al.* 2004). Their properties are studied well and worked out clearly. The microstrain and dislocation density are

calculated using the XRD parameters for these three samples. The PL studies show changes in optical properties, and the graph reveals that the property of the sample is moving towards the dopant from the base material state. ZnO is brighter than TiO_2 (Manish *et al.* 2012). The brightness of C is much less than the brightness of A. Hence, C is darker in nature in comparison with B as well as with A.

2. MATERIALS AND METHODS

2.1 Synthesis of the Sample

90% ZnO is mixed with 10% titanium dioxide; the medium used is the polar solvent (distilled water), and it is named A. Then 80% ZnO is mixed with 20% TiO_2. This combination is named B. Further, 70% ZnO is mixed with 30% TiO_2 and is named C. The sample is placed in a cool place; it's quite shady and dark. The sample is maintained below room temperature, below 30 degrees Celsius. The method used is the chemical vapor deposition method (Mohanpuria *et al.* 2010; Blessymol et al. 2023; Hema et al. 2025). The vapor is allowed to evaporate; the sample dries up due to the heat absorbed from the surroundings, and the sample itself has a molecular temperature. Because of this, the sample dries off, leaving the sediments (Mulvaney *et al.* 2002). The substrate used is a concave glass material; in the previous paper, this method is denoted as the concave dish method; moreover, it is a chemical vapor deposition method. The concept of using this method is to find out the change; the results clearly showed that this method elongates the bond length (Pillai and Kamat, 2004). The particles are larger compared to the other methods; the bandgap energy obtained is greater than that of the other methods. Even though the sizes obtained are bigger than those obtained by the other methods, the sizes do not exceed the nanoscale level; the results of the Scherrer method reveal this. Both amorphous materials are mixed in ratios and stirred for more than an hour and gently poured into the substrates, then subjected to vapor deposition for more than ten days in a cool atmosphere (Tan *et al.* 2003). The obtained samples are then used for further investigation and characterization.

3. RESULTS AND DISCUSSION

3.1 X-ray Diffraction

The XRD studies are taken for the three samples A, B, C, ZnO, and TiO_2. The graph shown in Fig. 1 reveals that the peak growth taken from the base material ZnO is seen in A, B, and C at a wavelength of 25 degrees. The adoption of the peaks from the dopant material could be seen at 31,33 and 36 degrees. These are the major peaks seen, and apart from them, peaks at wavelengths 46.9,56.5,62.7, and 68.56 degrees are obtained. The mentioned peaks are the shoot-up peaks, and apart from them, we can see many peaks. Moreover, each and every peak reveals important information (Kim *et al.* 2002). The wurtzite structure is linked with ZnO, and the anatase structure is linked with TiO_2.

Samples A, B, C, ZnO, and TiO_2 are combined and exhibit a single peak at 650 nm.

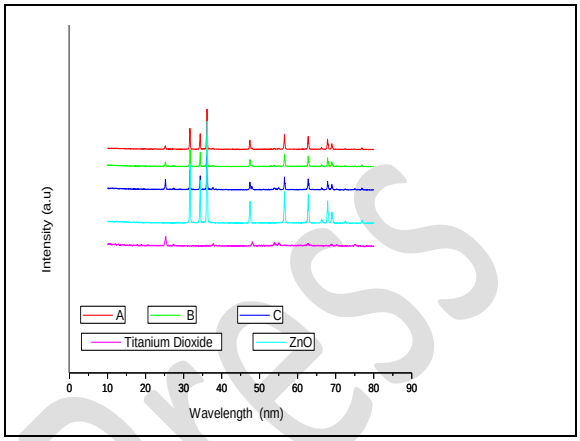

Fig. 1: XRD patterns of A, B, C, ZnO and titanium dioxide

Table 1. Comparison of samples A, B, C and their HKL plane values

S. No.	Sample A		Sample B		Sample C	
	Pos. [°2Th.]	HKL Planes	Pos. [°2Th.]	HKL Planes	Pos. [°2Th.]	HKL Planes
1	25.2425	101	25.2408	101	25.2388	101
2	31.6969	100	31.712	100	27.3344	110
3	34.3535	002	34.3609	002	31.7001	100
4	36.1825	101	36.1991	101	34.359	002
5	37.7188	101	37.6883	101	36.1928	101
6	47.4397	102	47.4695	102	37.7533	004
7	47.9469	102	48.0047	200	47.4464	102
8	53.8466	105	53.7696	211	47.9377	200
9	55.0185	211	55.03	211	53.8317	105
10	56.4941	110	56.4948	110	54.9911	211
11	62.7452	103	62.7585	211	56.4974	110
12	66.2511	112	66.2809	200	62.7568	103
13	67.8354	112	67.8463	116	62.9659	103
14	68.9818	112	68.0683	112	66.3305	200

15	72.4997	112	68.9716	116	67.8501	112
16	74.9607	103	70.2579	116	68.9734	201
17	76.8193	203	72.4931	110	70.3219	220
18	77.0803	110	75.0117	105	72.5419	004
19			76.8664	201	74.9862	215
20					76.8722	202

The samples A, B, and C exhibit a combination of the base material and the dopant. The size of the particles can be determined using TEM and SEM analysis; the Scherrer equation is used here in the theory. Using the Scherrer equation, the size of the particles is calculated. In my previous research paper, we used the Scherrer equation to calculate the size. There is a relation between the theta and the d parameters; as theta decreases, the related parameter d increases. This is a law-satisfying rule of Bragg's law. Hence, broadening of the peak is due to non-uniform strain, and deflection of the peak is due to uniform strain.

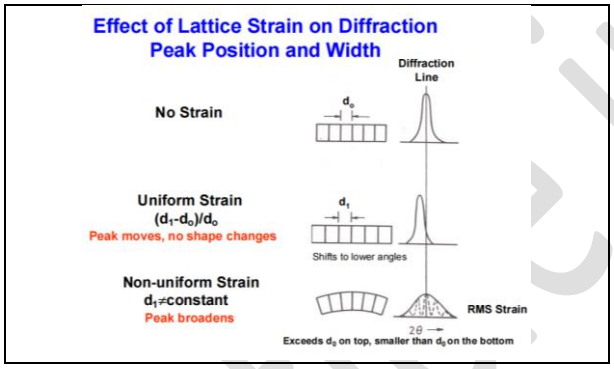

Fig. 1a: XRD graphs exhibiting peak position

Table 2. Comparison of samples ZnO, TiO_2 and their HKL plane values

S. No.	ZnO		TiO_2	
	Pos. [°2Th.]	HKL Planes	Pos. [°2Th.]	HKL Planes
1	25.2425	101	25.2408	101
2	31.6969	100	31.712	100
3	34.3535	002	34.3609	002
4	36.1825	101	36.1991	101
5	37.7188	101	37.6883	101
6	47.4397	102	47.4695	102
7	47.9469	102	48.0047	200
8	53.8466	105	53.7696	211
9	55.0185	211	55.03	211
10	56.4941	110	56.4948	110
11	62.7452	103	62.7585	211
12	66.2511	112	66.2809	200
13	67.8354	112	67.8463	116
14	68.9818	112	68.0683	112
15	72.4997	112	68.9716	116
16	74.9607	103	70.2579	116
17	76.8193	203	72.4931	110
18	77.0803	110	75.0117	105
19			76.8664	201

The JCPDS card number is JCPDS 36-1451 for the hexagonal wurtzite structure of ZnO; then, for TiO2 (anatase) tetragonal structure, the JCPDS card number is JCPDS 21-1272. On scaling the plot for A, B, C, ZnO, and TiO_2, the XRD reveals its intensity change over. This intensity changeover is clearly shown in Figure 1c.

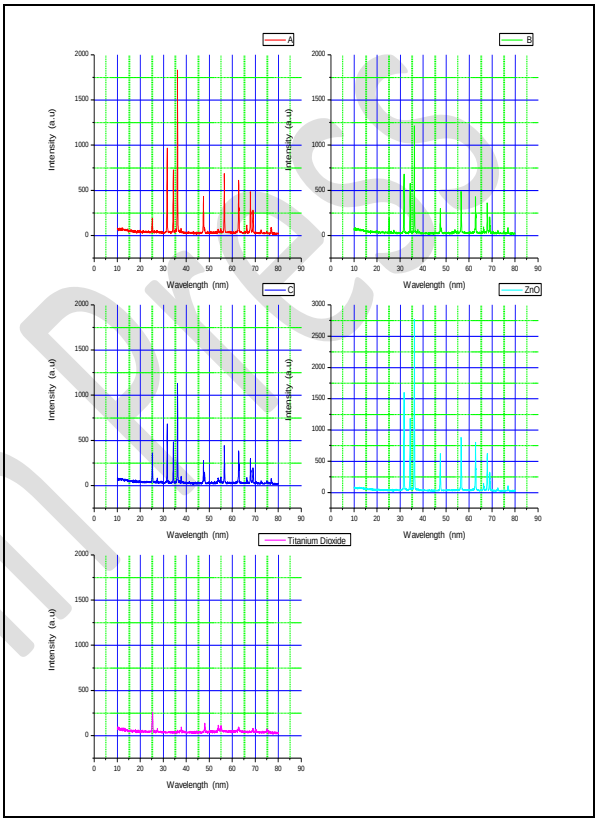

Fig. 1c: XRD patterns of A, B, C, ZnO and titanium dioxide

3.2 Photoluminescence Analysis

The PL analysis is a technique used to analyze the electronic, optical, and structural properties of materials by using light as the source (Li *et al.* 2006). The light source excites the sample to produce secondary photons. Photoluminescence can be divided into major segments: one is fluorescence, and the other is phosphorescence (Li *et al.* 2004). The optical property of ZnO is higher in comparison with TiO_2. The photoluminescence study of A is more or less equal to ZnO, whereas upon doping with the dopant, the intensity of the sample gets reduced according to the concentration of the doping nature (Aman *et al.* 2023). As the (Fig. 2), clearly reveals the intensity change caused by doping, from 350 nm to 600 nm wavelength the intensity graph of the samples, exhibit their relevance and irrelevance (Jiang *et al.* 2024). But exactly at 800 nm, it shows a sharp peak. Samples A, B, C, ZnO, and TiO_2 are

combined and show up as a single peak; the intensity is at 650 nm. The photon excitation happens at 380 nm (Cychosz *et al.* 2017).

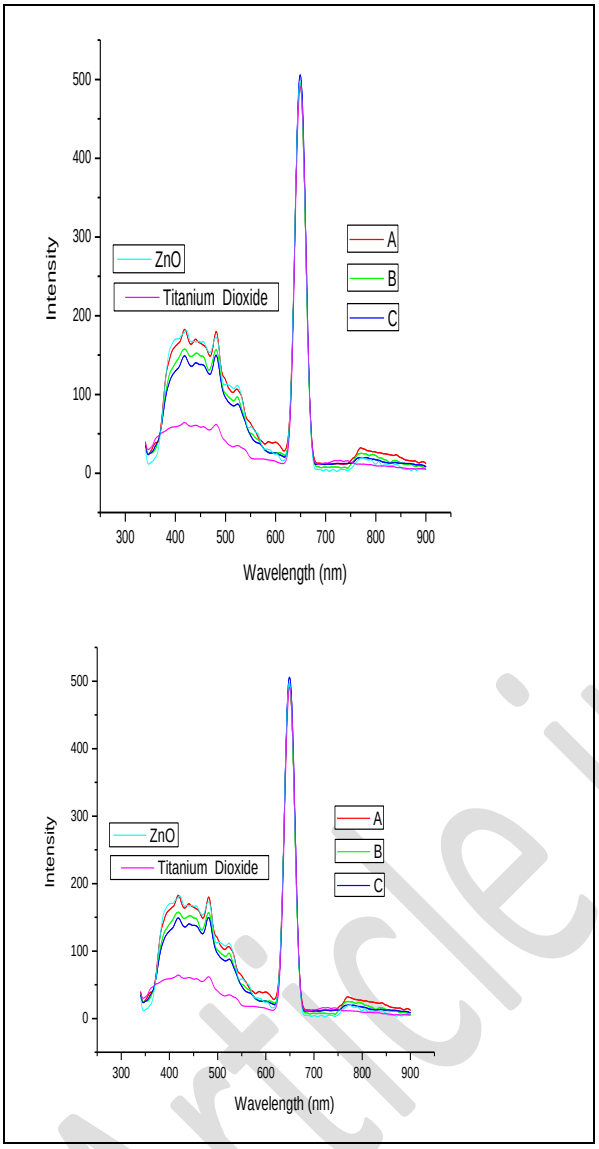

Fig. 2: Photoluminescent patterns of A, B, C, ZnO and titanium dioxide

The sharp peak denotes that the crystallinity is pure (Sorarù *et al.* 1995). The broad peaks exhibit structural changes or a shift in their position in the case of structure (Niemiec *et al.* 2018). The drop in the peak from 550 nm to 640 nm reveals that the charge carriers are getting separated. Either the charge carriers get locked in the bond spaces, or they are unable to leave the place due to the existence of defects in the sample (Feng *et al.* 2015).

3.3 UV Analysis

The optical property of ZnO is high in comparison with TiO_2. The absorbance property increases when the dopant level increases. This clearly indicates that the colour of sample C is darker than sample A. This observation tells us that the absorption property of TiO_2 is greater in comparison to ZnO (Wu *et al.* 2014).

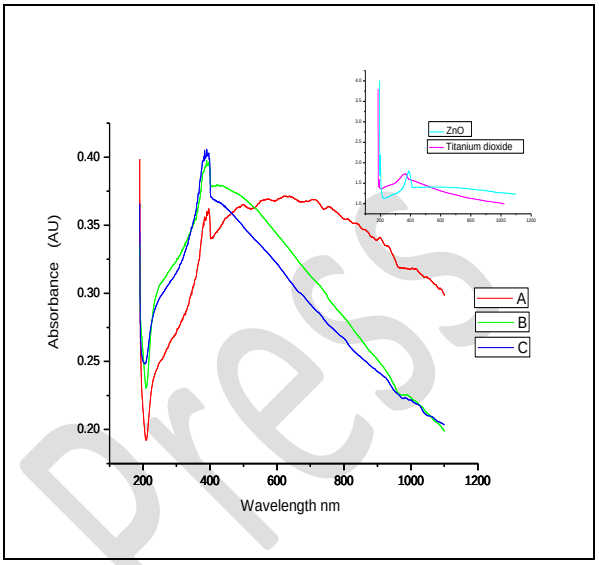

Fig. 3: UV patterns of A, B, C, ZnO, and titanium dioxide

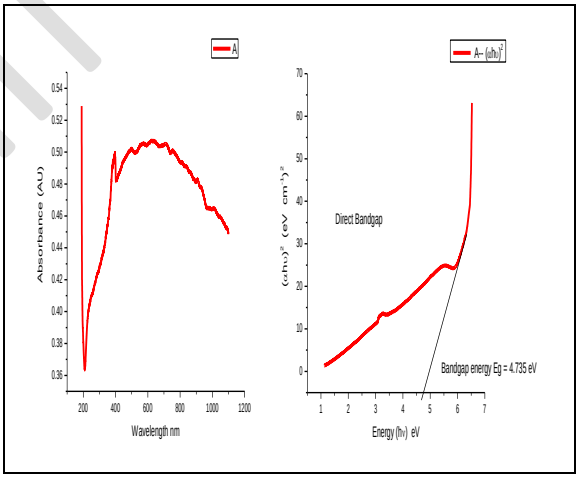

Fig. 3a: UV patterns of A and energy bandgap

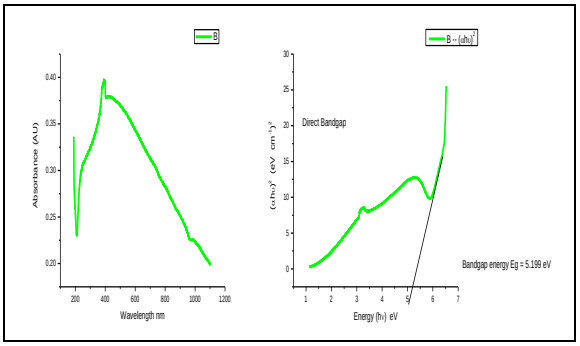

Fig. 3b: UV patterns of B and energy bandgap

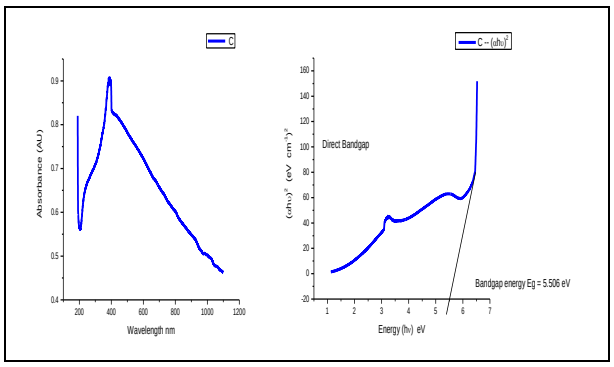

Fig. 3c: UV patterns of C and energy bandgap

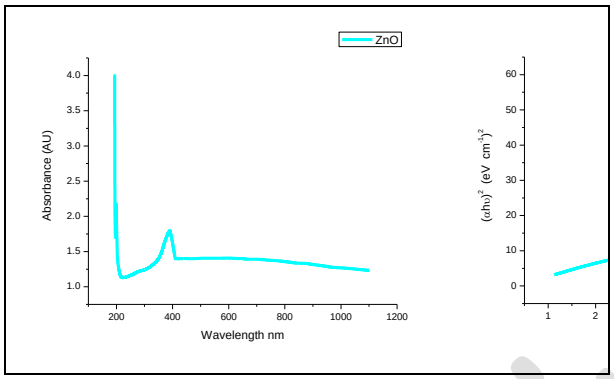

Fig. 3d: UV patterns of ZnO and energy bandgap

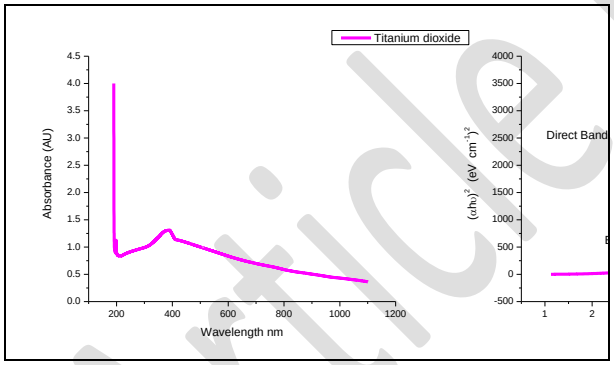

Fig. 3e: UV patterns of TiO_2 and energy bandgap

The size of the particle increases gradually; this indicates that the lattice structure changes. The intermolecular distance increases in the lattice arrangement (Dai *et al.* 2025). The material or the sample is trying to reach the performance of an insulator, as standard insulators have an energy band gap starting from 3eV to 6 eV. As the size of the particle increases, the energy band gap increases, but here both parameters are increasing. This is due to the substrate used; elongation of the intermolecular structures is the reason behind it (Wang *et al.* 2024).

3.4 FTIR Analysis

The FTIR pattern of A exhibits 9 peaks, the FTIR pattern of B exhibits 10 peaks, the FTIR pattern of C exhibits 11 peaks, the FTIR pattern of ZnO exhibits 9 peaks, and finally the FTIR pattern of TiO_2 exhibits 4 peaks.

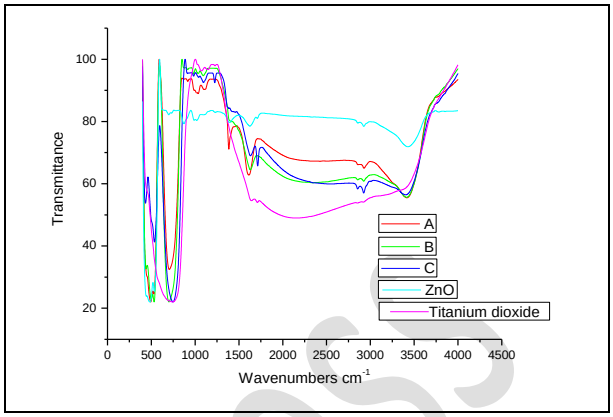

Fig.4: FTIR pattern of A, B, C, ZnO and titanium Dioxide

The transmittance level of ZnO is greater in comparison to TiO_2; this could be figured out in the region between 2225 cm-1 and 3225 cm^{-1} (Vijayakumar *et al.* 2021). As the concentration of the dopant increases, the transmittance level of the sample decreases; the entire sample is trying to reach the dopant level (Niemiec *et al.* 2018). The absorbance property of TiO_2 is greater compared to ZnO (Rani *et al.* 2023).

3.5 Raman Analysis

The Raman analysis is a non-destructive technique; it is used to find out the chemical structures, then to identify the polymorphs, and finally the molecular interactions by analyzing the inelastic scattering (Raman effect) from a source, which is a laser. Elastic scattering is Rayleigh (green), but the inelastic scattering is Raman (red/blue) (Feng *et al.* 2015). The peaks of ZnO are greater in comparison to TiO_2; this could be figured out in the region between 2225 cm-1 and 3225 cm^{-1}. As the concentration of the dopant increases, the transmittance level of the sample decreases; the entire sample is trying to reach the dopant's original form (Wu et al., 2014).

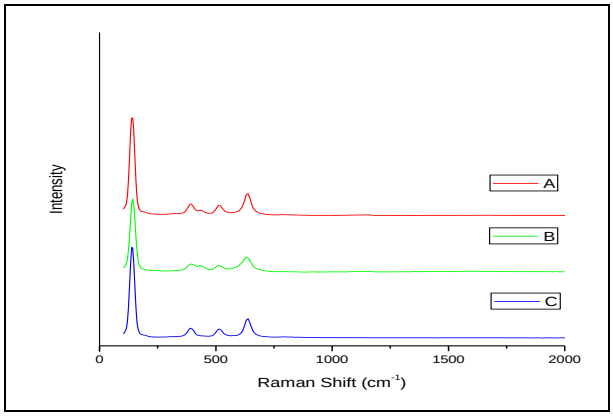

Fig. 10a: Raman spectrum of A, B, C

A change can be seen in the range from 375 nm to 450 nm as the concentration increases. A peak seen at 430 nm for samples A and B disappears in graph C. This clearly indicates that the doping has led to the Raman shift.

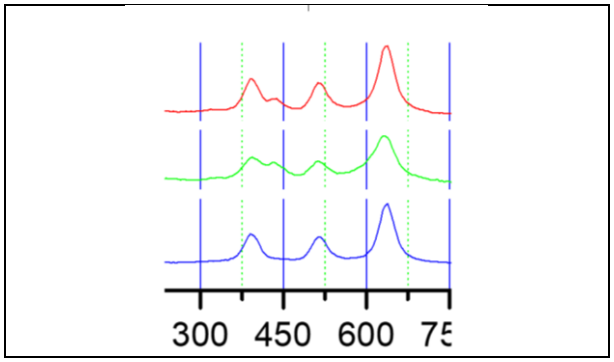

Fig. 10b: Raman spectrum of A, B, C

The Raman spectrum exhibits a fine change from 250 cm^{-1} to 500 cm^{-1}.

3.6 Scherrer Method and Williamson-Hall Plot Analysis

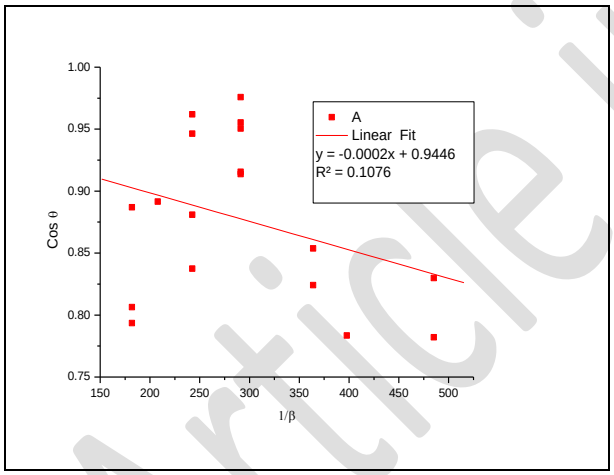

Fig. 11: Scherrer plot for A nanoparticles

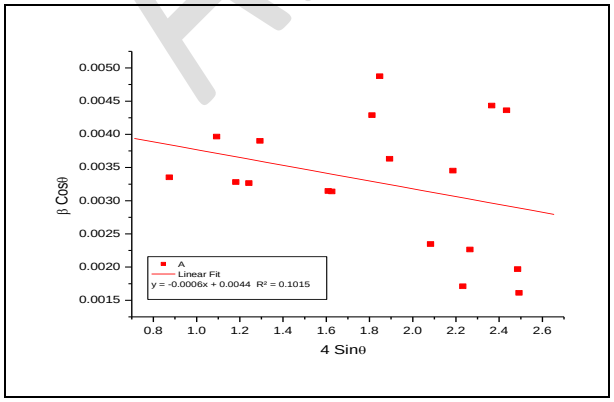

Fig. 12: Williamson-Hall plot for A nanoparticles

The accuracy is more or less matching; this could be achieved with fine conditions in which both exhibit a more negative value (Dai *et al.* 2025). There is no major change between the Scherrer and the Williamson-Hall plot. The error approximation seen in the case of the data overlooks the perfection of the XRD data (Wang *et al.* 2024). As the concentration of the dopant in the base material is increased, the linear fit line shown in the analysis changes from negative to positive. This proves that the sample changes from a negative inclination to a positive inclination (Li *et al.* 2023).

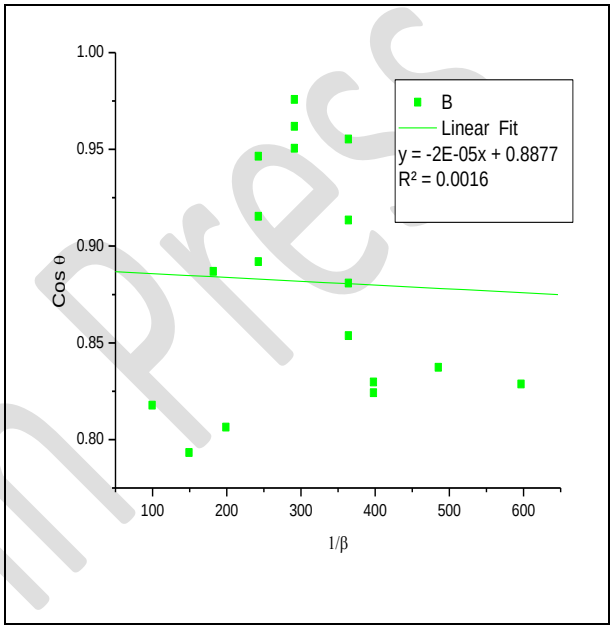

Fig. 13: Scherrer plot for B nanoparticles

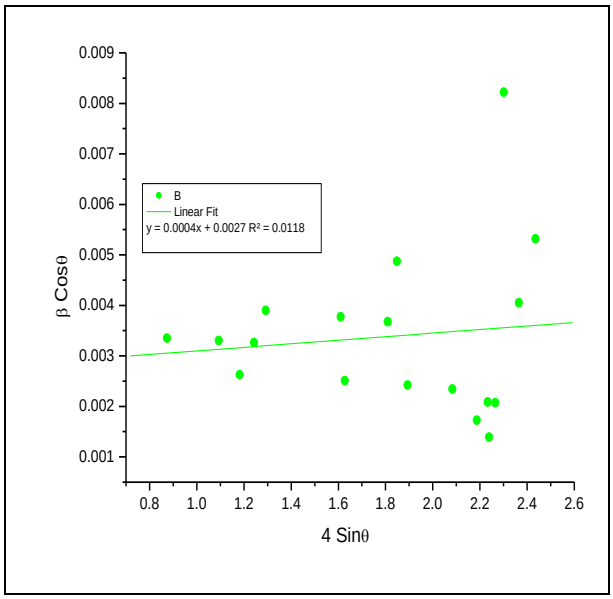

Fig. 14: Williamson-Hall plot for B nanoparticles

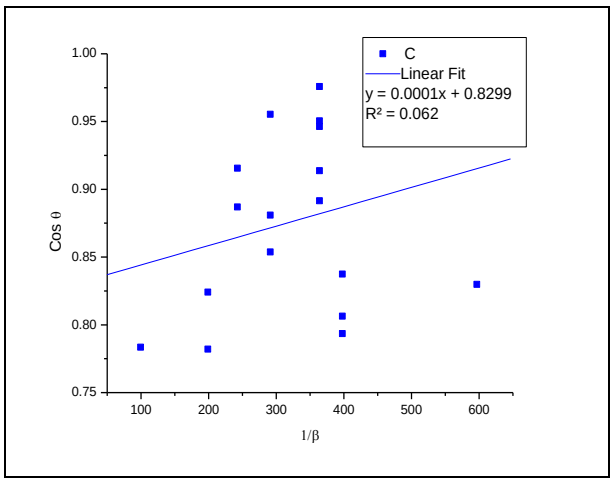

Fig. 15: Scherrer plot for C nanoparticles

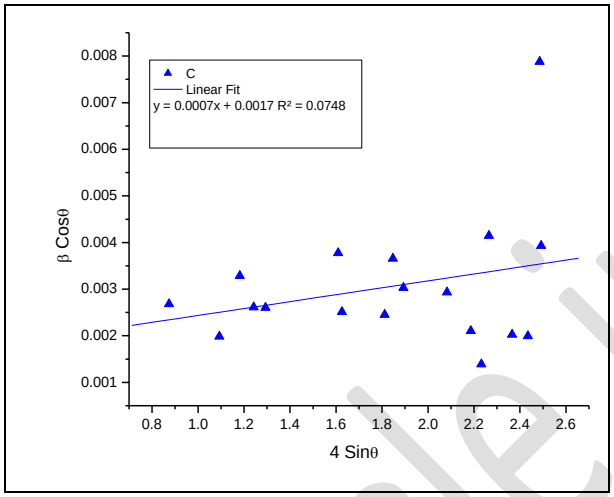

Fig. 16: Williamson-Hall plot for C nanoparticles

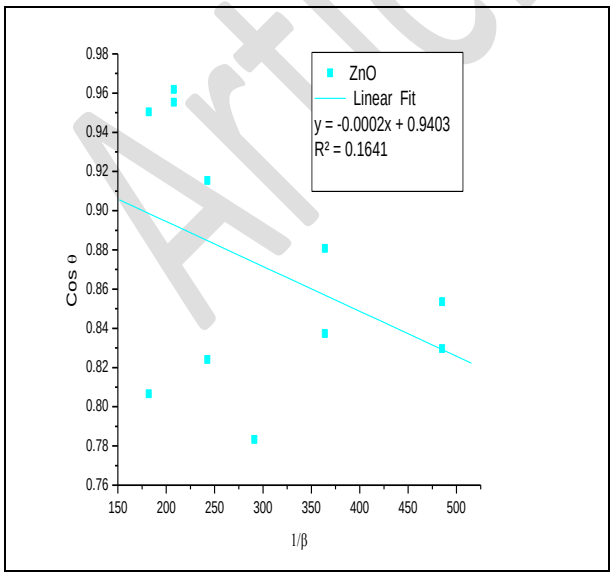

Fig. 17: Scherrer plot for ZnO nanoparticles

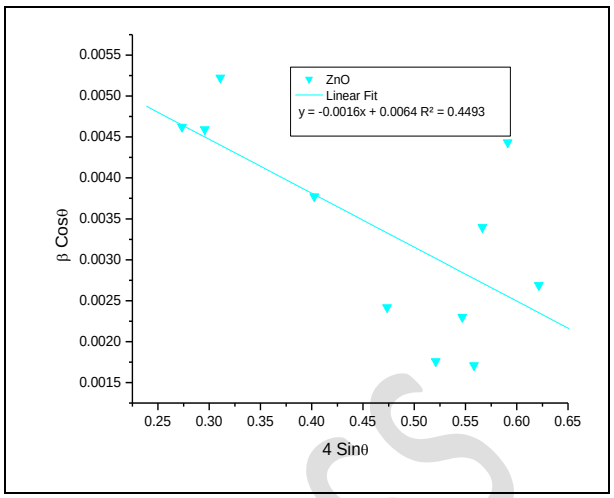

Fig. 18: Williamson-Hall plot for ZnO nanoparticles

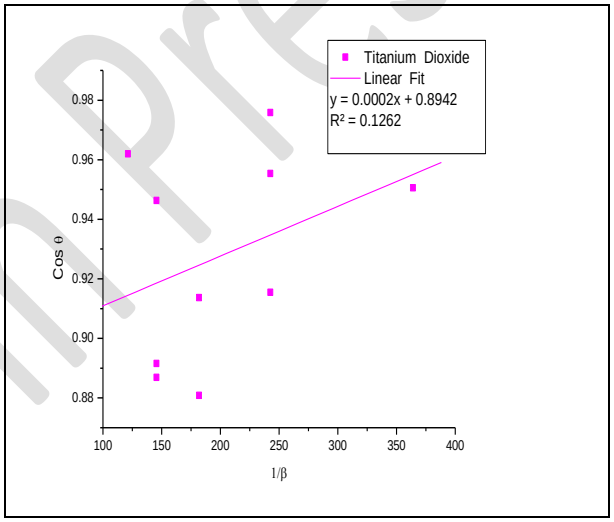

Fig. 19: Scherrer plot for titanium dioxide nanoparticles

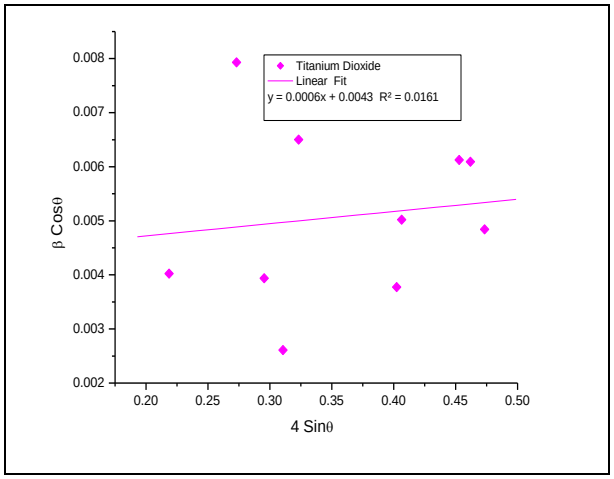

Fig. 20: Williamson-Hall plot for titanium dioxide nanoparticles

Table 3. Size of the Particle, dislocation density and microstrain

S. No.	Composition	Particle Size	Dislocation Density (S)	Micro Strain €
1	A	46.93352	6.04938	0.81931
2	B	48.8556	7.224169	0.845972
3	C	52.20624	5.845832	0.763588
4	ZnO	47.68088	7.26386	0.769376
5	Titanium Dioxide	29.99272	8.127876	1.271616

Negative slope indicates that a lattice contraction or lattice strain occurs due to compression, and a positive slope indicates lattice elongation or expansion (Dai *et al.* 2025). As the d-spacing changes, the d-spacing gets reduced. The dopant used might induce the property of elongation. Taking out the outlined plots can shoot up the R^2 value to 0.9 in the linear fit. These are the errors; by removing them, we could shoot up the R^2 value (Rwenyagila, 2017).

3.7 CV Analysis

The process of voltage versus current is the idea behind cyclic voltammetry; direct current (DC) is used. This is a technique specifically known as an electroanalytical technique (Hagberg *et al.* 2007). This is used to analyze the reduction and oxidation process, known as redox, of an examined molecular species by scaling the current response to a set of potential values. The graph exhibits the anodic peak current i_{pa}, anodic peak voltage E_{pa} (Scharber and Sariciftci, 2021). Then the cathodic peak current i_{pc}, and the cathodic peak voltage E_{pc}. In all the graphs, it is clearly seen that the reversible reaction and the quasi-reversible reaction are clearly exhibited; however, the irreversible reactions are not exhibited (Wang *et al.* 2018). The conductivity is good and excellent in the case of ZnO compared to Titanium dioxide. For 600 mV, the peak current is only 120 mA, but in the case of ZnO it is nearly 250 mA at 600 mV. Upon doping, the current value changes as the concentration increases (Costa *et al.* 2016). The formal potential EO ' can be calculated from Equation 1.

$$EO' = (E_{pa} + E_{pc})/2 \quad \ldots (1)$$

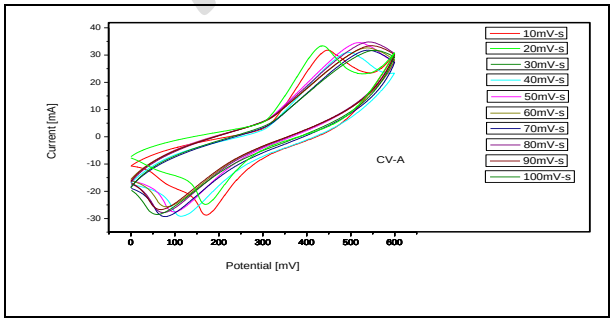

Fig. 21: CV analysis of A nanoparticles

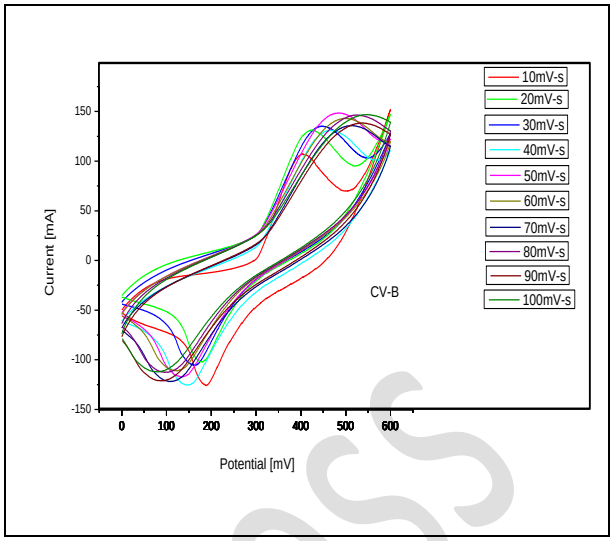

Fig. 22: CV analysis of B nanoparticles

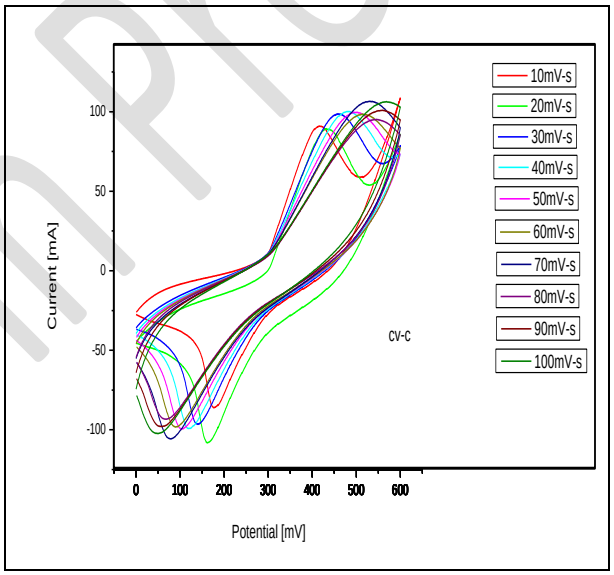

Fig. 23: CV analysis of C nanoparticles

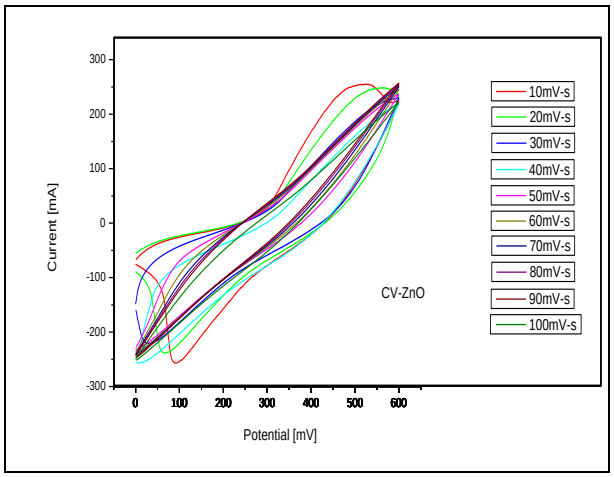

Fig. 24: CV analysis of ZnO nanoparticles

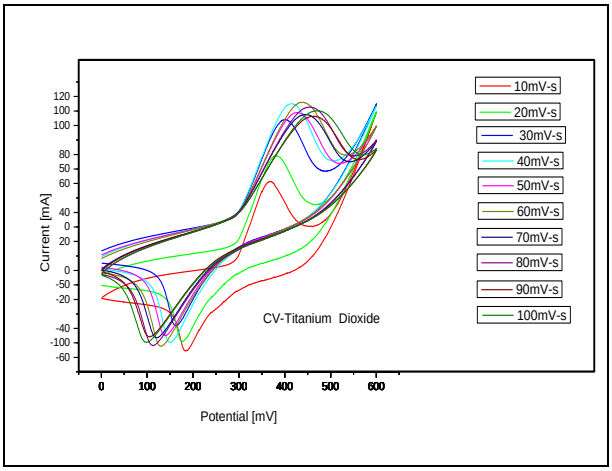

Fig. 25: CV analysis of titanium dioxide

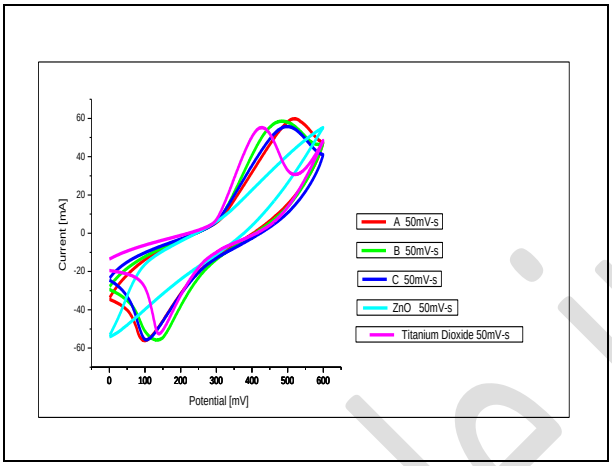

Fig. 26: CV analysis of A, B, C, ZnO and titanium dioxide nanoparticles

3.8 EIS Analysis

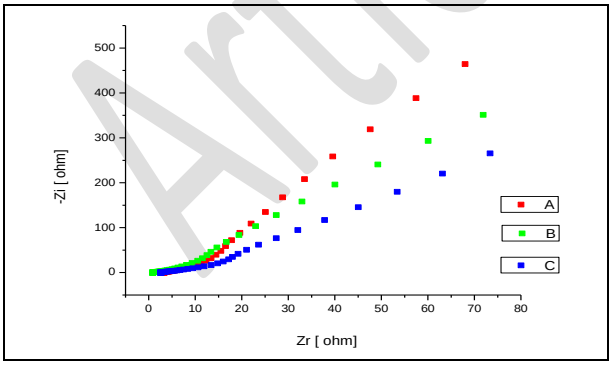

Fig. 27: Electrochemical impedance spectroscopy of A, B, C

The Electrochemical Impedance spectroscopy data, or the graph, reveals that sample A has higher impedance in the case of -Z compared to sample C. Alternating current is used in this analysis technique (Christensen *et al.* 2020).

3.9 DSC, TGA-DTA Analysis

The DSC and TGA-DTA patterns are shown in Fig. 28 to Fig. 31; here, a basic introduction to the concept is given in the initial state. DSC is a technique, specifically known as a thermoanalytical technique (Gopinath *et al.* 2012). This technique measures the amount of heat released or absorbed by the irradiated sample when it is heated or cooled, or when kept at a constant temperature (Mustakim *et al.* 2021). The sample is compared with the reference material, and the details are retrieved; this predominantly determines the occurrence of melting, crystallization, and glass transition in the sample caused by the application of heat (Nazari and Shadi, 2022). In the case of DSC, the sample is treated with heat; this brings about a change in the thermal transition of the sample or the material. DSC measures the heat flux; in addition, the enthalpy changes are taken into account (Tanimola and Steve, 2024). The obtained graphs give us a report that it is exposed. The physical state of the sample does change, and the internal chemical state also changes. To find the thermal stability of the sample or the material, differential thermal analysis (DTA) and thermogravimetric analysis (TGA) are applied to the sample (Tsampali *et al.* 2025).TGA examines the concept of weight reduction or accumulation due to heat applied to the sample at a given temperature. TGA is a well-known technique which measures the change in mass or weight reduction when the sample is subjected to heat or cooling or when held at constant pressure in a controlled state (Yu *et al.* 2026). This ensures thermal stability and kinetics in terms of decomposition, moisture or solvent content. DTA is a famous thermoanalytical technique that focuses on the parameter ΔT (difference in temperature); the difference in temperature is taken between the reference and the sample (Zhan *et al.* 2022). The sample is subjected to heating or cooling (Senff *et al.* 2009). This technique identifies exothermic (heat-releasing) and endothermic (heat-absorbing) processes (Shafi *et al.* 2016). The obtained details exhibit melting, crystallization behavior, and phase transitions. A clear study can be inferred from the obtained details.

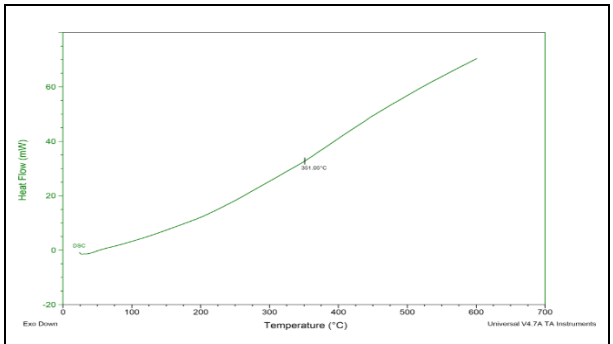

ZnO DSC

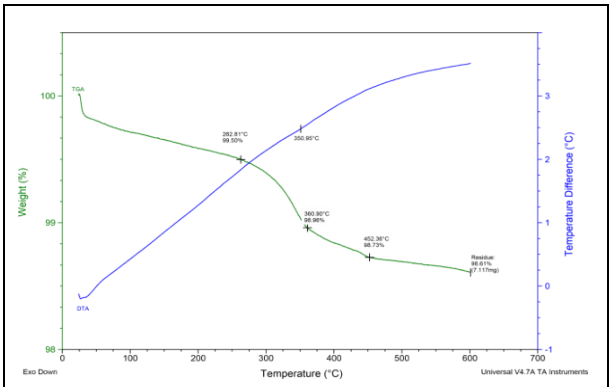

TGA-DTA

Fig. 28: DSC, TGA-DTA of ZnO

The material ZnO exhibits a change in its melting point at 351.05 (OC), as the temperature is increased, the heat flow through the material or the sample also increases (Zhang *et al.* 2012). This proves that the base material ZnO is a good conductor of heat. The TGA graph reveals the weight loss of ZnO as the temperature is increased on the sample (Sarkaraisamy *et al.* 2026). At three major points, it exhibits physical changes, that is, at 262.81 (^{O}C), 360.90 (^{O}C) and 452.36 (^{O}C).

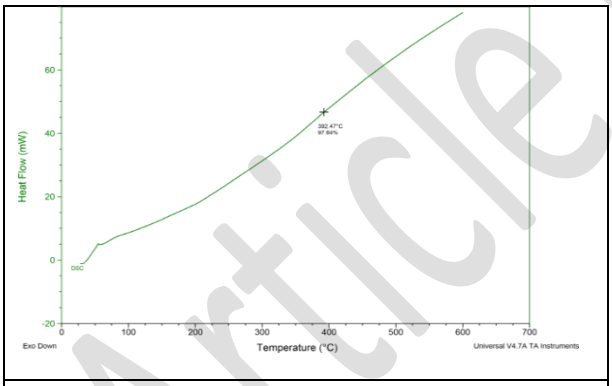

Titanium Dioxide DSC

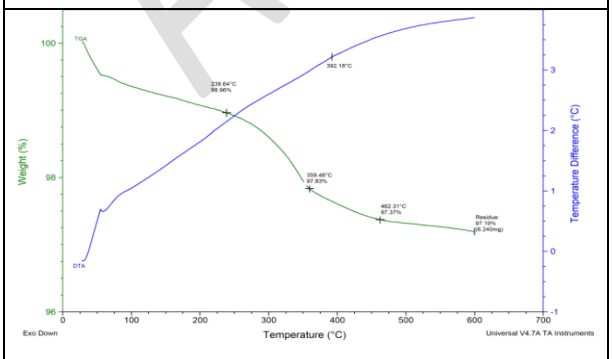

TGA-DTA

Fig. 29: DSC, TGA-DTA of titanium dioxide

Here, the DSC graph exhibits the phase transition details; it can be seen that it occurs at 392.42 (O C). Titanium dioxide is a good conductor of heat. At three major points, it exhibits physical changes, which are at 238.64 (^{O}C), 359.48 (^{O}C) and 462.31 (^{O}C) (Katika and Boddu, 2025).

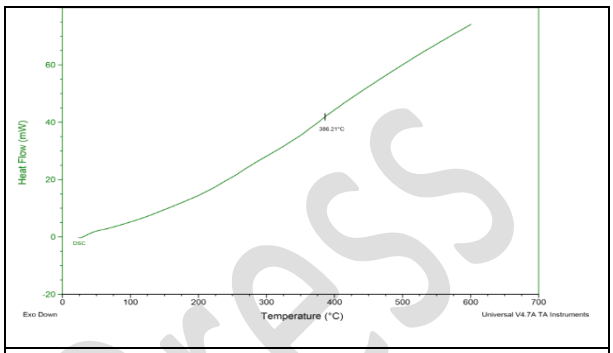

A DSC

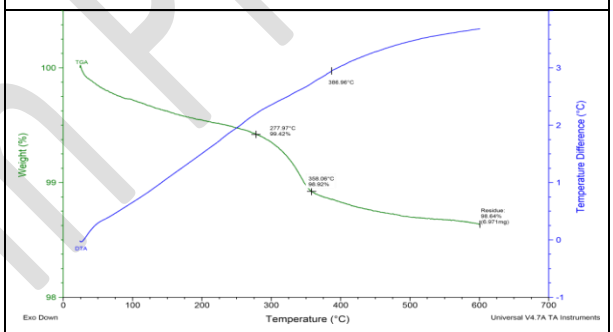

TGA-DTA

Fig. 30: DSC, TGA-DTA of A

The DSC graph exhibits the phase transition details; it can be seen that it occurs at 386.21 (OC). Titanium dioxide is a good conductor of heat. At two major points, it exhibits physical changes, which are at 277.97 (^{O}C) and 358.06 (^{O}C) (Koutenaei *et al.* 2022).

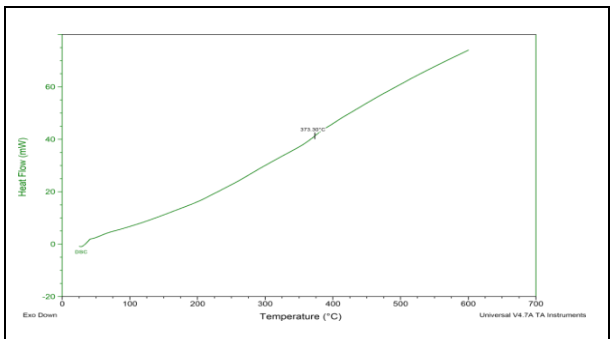

B DSC

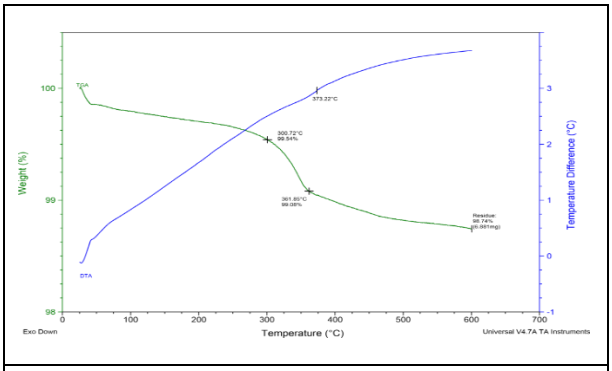

TGA-DTA

Fig. 31: DSC, TGA-DTA of B

The DSC graph exhibits the phase transition details; it can be seen that it occurs at 373.30 (OC). Titanium dioxide is a good conductor of heat (Li *et al.* 2026). At two major points, it exhibits physical changes, which are at 300.72 (^{O}C) and 361.85 (^{O}C).

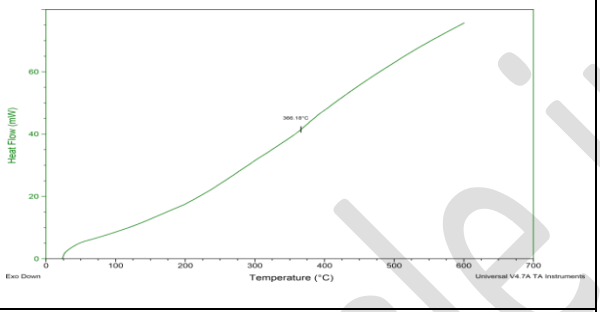

C DSC

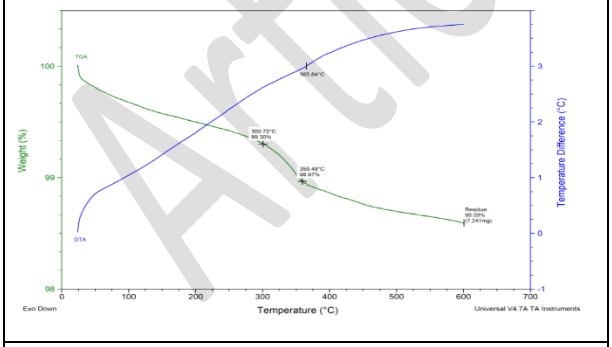

TGA-DTA

Fig. 32: DSC, TGA-DTA of C

The DSC graph exhibits the phase transition details; it can be seen that it occurs at 366.18 (OC). Titanium dioxide is a good conductor of heat (Morsch *et al.* 2016). At two major points, it exhibits physical changes, which are at 300.72 (^{O}C) and 359.48 (^{O}C).

Table 4. DSC, DTA and residues of ZnO, TiO_2, A, B and C

S. No		DSC	DTA	Residue	
1	ZnO	351.05	350.95	98.61	7.117 mg
2	TiO_2	392.47	392.18	97.19	6.240 mg
3	A	386.21	386.96	98.64	6.971 mg
4	B	373.3	373.22	98.74	6.881 mg
5	C	366.18	365.64	98.59	7.241 mg

Table 5. Temperature, TGA and weight percentage of ZnO, TiO_2, A, B, and C

S. No		Temperature Degrees Celsius	TGA	Weight Percentage
1	Zno	260	262.81	99.5
		360	360.9	98.96
		450	452.36	98.73
2	TiO_2	232	238.64	98.96
		355	359.48	97.83
		470	462.31	97.37
3	A	275	277.97	99.42
		356	358.06	98.92
4	B	300	300.72	99.54
		360	361.85	99.08
5	C	300	300.72	99.3
		360	359.48	98.97

The ability of a material to withstand high temperatures indicates that the material has bonds which are stable and flexible (Mridha *et al.* 2025). The restoration to the original state is quite predominant. Moreover, the elastic nature of the bonds is stable for thermal inclusion.

4. CONCLUSION

The nature of the materials like ZnO and TiO_2 is well identified; the mixed nature shows its behaviour. The intensity of the dopant has a regular effect on the base material. Each and every characterization study narrates the peculiar effect caused by the dopant on the regular base material. The plots shown in the Williamson-Hall and the Scherrer reveal that the dopant has the effect of changing the linear fit axis line; it proves that the negative entity moves towards the positive identity.

FUNDING

This research received no specific grant from any funding agency in the public, commercial, or not-for-profit sectors.

CONFLICTS OF INTEREST

The authors declare that there is no conflict of interest.

COPYRIGHT

REFERENCES

Aman, S., Alhmari, S. D., Khan, S. A., Abdullah, A. G., Ejaz, S. R., Ahmad, N., Alharbi, F. F., Asma, S. and Farid, H. M. T., Hydrothermal Development of Bimetallic Sulfide Nanostructures as an Electrode Material for Supercapacitor Application, *Energy Fuels*, 37(22), 17473-17483(2023). https://doi.org/10.1021/acs.energyfuels.3c03380

Blessymol. B, Kalaiselvi. V, Yasotha. P, Gopi. S, Comparative Study of Chemically and Green Synthesized Titanium Dioxide Nanoparticles using Leucas aspera Leaf Extract, J. Environ. Nanotechnol., 12 (3), 10- 13 (2023). https://doi.org/10.13074/jent.2023.09.233471

Brust, M. and Kiely, C. J., Some recent advances in nanostructure preparation from gold and silver particles: a short topical review, *Coll. Surf. A: Phys. Chem. Eng. Asp.*, 202(2-3), 175-186 (2002). https://doi.org/10.1016/S0927-7757(01)01087-1

Christensen, T. H., Damgaard, A., Levis, J., Zhao, Y., Bjorklund, A., Arena, U., Barlaz, M. A., Starostina, V., Boldrin, A., Astrup, T. F. and Bisinella, V., Applicaation of LCA modelling in integrated waste management, *Waste Manage*., 118, 313-322(2020). https://doi.org/10.1016/j.wasman.2020.08.034

Costa, J. C. S., Taveira, R. J. S., Lima, C. F. R. A. C., Mendes, A. and Santos, L. M. N. B. F., Optical band gaps of organic semiconductor materials, *Opt. Mater. (Amst).*, 58, 51–60 (2016). https://doi. org/10.1016/j.optmat.2016.03.041

Cychosz, K. A., Nicolas, G. R., Javier, G. M. and Thommes, M., Recent advances in the textural characterization of hierarchically structured nanoporous materials, *Chem. Soc. Rev*., 46(2), 389-414(2017). https://doi.org/10.1039/C6CS00391E

Dai, T., Meng, Y., Wang, Z., Lu, J., Zhi, Z., Du, M., Guo, Q. and Zhou, E., Modulation of molecular quadrupole moments by phenyl side-chain fluorination for high-voltage and high-performance organic solar cells, *J. Am. Chem. Soc*., 147(5), 4631–4642 (2025). https://doi.org/10.1021/jacs.4c17140

Feng, J., Feng, J., Xiao, Y. and Jiang, Y., Synthesis, structure, and properties of silicon oxycarbide aerogels derived from tetraethylortosilicate /polydimethylsiloxane, *Ceram. Int.*, 41(4), 5281–5286 (2015). https://doi.org/10.1016/j.ceramint.2014.11.111

Gopinath, S., Mouli, P. C., Murthy, A. R., Iyer, N. R. and Maheswaran, S., Effect of Nanosilica on Mechanical Properties and Durability of Normal Strength Concrete, *Arch. Civ. Eng.*, 58(4), 433–444(2012) https://doi.org/10.2478/v.10169-012-0023-y

Guenther, B., Kumpmann, V. and Kunze, H. D., Secondary recrystallization effects in nanostructured elemental metals, *Scr. Met. Mat*., 27(7), 833-838 (1992). https://doi.org/10.1016/0956-716X(92)90401-Y

Hagberg, D. P., Tannia, M., Karl, K. M., Nonomura, K., Qin, P., Gerrit, B., Tore, B., Andres, H. and Sun, L., Tuning the HOMO and LUMO energy levels of organic chromophores for dye sensitized solar cells. *J. Org. Chem. Dec.*, 72(25), 9550–9556 (2007). https://doi.org/10.1021/jo701592x

Hema. K, Anishia. S. R., Rajeswari. S, Padmavathy V, Sujatha. S, Thiyagu. M, Green Synthesis and Multifunctional Applications of Moringa Oleifera-enhanced TiO2 Nanocomposites, J. Environ. Nanotechnol., 14 (1) 7-17 (2025). https://doi.org/10.13074/jent.2025.03.2511225

Jiang, L., Shi, H., Han, M., Zhang, Y., Liang, J., Chen, J., Geng, S., Tong, L. and Sheng, L., Rearrangement of pore Structure-Enabled Micropore-Dominant N, O Co-Doped carbon for ultrafast Charge/Discharge rate supercapacitors at Commercial-Scale mass loading, *ACS Sustainable Chem. Eng*., 12(51), 18422-18433 (2024). https://doi.org/10.1021/acssuschemeng.4c07871

Katika, R. M. and Boddu, S., Synthesis and Characterization of Nanobiochar for Enhanced Photo Decolouration of Azoic Dye, *J. Instit. Eng. (India): Series E*, 106(2), 115–128 (2025). https://doi.org/10.1007/s40034-025-00304-7

Kim, D. O., Lee, K. W., Lee, H. J., and Lee, C. Y., Vitamin C equivalent antioxidant capacity (VCEAC) of phenolic phytochemicals, *J. Agric. Food Chem*., 50, 3713–3717 (2002). https://doi.org/10.1021/jf020071c

Koutenaei, S. S., Vatankhah, G. and Esmaeili, H., Ziziphus spina-christi Leaves Biochar Decorated with Fe_3O_4 and SDS for Sorption of Chromium (III) from Aqueous Solution, *Biomass Convers. Biorefine.*, 14(9), 10251–10264 (2022). https://doi.org/10.1007/s13399-022-03029-4

Li, J., Lin, Y. and Zhao, B., Spontaneous Agglomeration of Silver Nanoparticles Deposited on Carbon Film Surface, *J. Nanoparticle Res*., 4(4), 345-348 (2002). https://doi.org/10.1023/A:1021120723498

Li, L., Sun, X., Yang, Y., Guan, N. and Zhang, F., Synthesis of anatase TiO_2 nanoparticles with beta-cyclodextrin as a supramolecular shell, *Chem. Asian*

J., 1(5), 664-668(2006). https://doi.org/10.1002/asia.200600103

Li, P., Liu, Y., Sun, Y. and Zhang, C., Biochar Innovations for Organic Pollutant Remediation in Contaminated Soils, *Mol.*, 31(3), 432(2026). https://doi.org/10.3390/molecules31030432

Li, X., Tang, A., Wang, H., Wang, Z., Du, M., Guo, Q., Guo, Q. and Zhou, E., Benzotriazole-based 3D four-arm small molecules enable 19.1% efficiency for PM6: Y6-based ternary organic solar cells. *Wiley Angew. Chem. Int. Ed. Engl*., 62(39), e202306847(2023). https://doi.org/10.1002/anie.202306847

Li, Y., White, T. J. and Lim, S. H., Low-temperature synthesis and microstructural control of titania nano-particles, *J. Sol. State Chem*., 177(4-5), 1372-1381 (2004). https://doi.org/10.1016/j.jssc.2003.11.016

Manish, H., Shreeram, J., Mayur, D. and Kisan, K., Green synthesis of TiO_2 nanoparticles by using aqueous extract of Jatropha curcas L. Latex, *Mater. Lett*., 75, 196–199 (2012). https://doi.org/10.1016/j.matlet.2012.02.018

Mohanpuria, P., Rana, N. K. and Yadav, S. K., Biosynthesis of nanoparticles: Technological concepts and future applications, *J. Nanoparticle Res*., 10(3), 507–517 (2010). https://doi.org/10.1007/s11051-007-9275-x

Morsch, S., Liu, Y., Greensmith, P., Lyon, S. B. and Gibbon, S. R., Molecularly Controlled Epoxy Network Nanostructures, *Polym.*, 108, 146–153(2016). https://doi.org/10.1016/j.polymer.2016.11.050

Mridha, D., Lamsal, B. and Antonangelo, J. A., Nanotechnology in Agriculture: Innovations for Sustainability and Greenhouse Gas Mitigation—A Review, *Sci. Tot. Environ*., 995, 180065 (2025). https://doi.org/10.1016/j.scitotenv.2025.180065

Mulvaney, P., Wilson, O. and Wilson, G. I., Laser Writing in Polarized Silver Nanorod Films, *Adv. Mater*., 14(13-14), 1000-1004 (2002). https://doi.org/10.1002/1521-4095(20020705)14:13/14<1000::AID-ADMA1000>3.0.CO;2-E

Mustakim, S. M., Das, S. K., Mishra, J., Asif, A., Thamar, A. S., Hasan, A. S. and Kaze, C. R., Improvement in Fresh, Mechanical and Microstructural Properties of Fly Ash- Blast Furnace Slag Based Geopolymer Concrete by Addition of Nano and Micro Silica, *Silicon*, 13(8), 2415–2428(2021). https://doi.org/10.1007/s12633-020-00593-0

Nazari, A. and Shadi, R., Retraction Note to: Effects of CuO Nanoparticles on Compressive Strength of Self-compacting concrete, *Sadhana*, 47, 264(2022). https://doi.org/10.1007/s12046-022-02043-6

Niemiec, W., Szczygieł, P., Jeleń, P. and Handke, M., IR investigation on silicon oxycarbide structure obtained from precursors with 1:1 silicon to carbon atoms ratio and various carbon atoms distribution, *J. Mol. Struct*., 1164, 217–226(2018). https://doi.org/10.1016/j. molstruc.2018.03.046

Pillai, Z. S. and Kamat, P. V., What Factors Control the Size and Shape of Silver Nanoparticles in the Citrate Ion Reduction Method, *J. Phys. Chem. B*., 108(3), 945-951 (2004). https://doi.org/10.1021/jp037018r

Rwenyagila, E., A review of organic photovoltaic energy source and its technological designs, *Wiley Int. J. Photoenergy*, 2017(1), 1656512 (2017). https://doi.org/10.1155/2017/ 1656512

Sarkaraisamy, P., Kannan, E. P., Prasanth, V., Gopal, J., Sarkaraisamy, P. and Muthu, M., Antimicrobial Resistance Status of Small Marine Fishes off the Coastal Cities of East and West Coast of India: An Adaptive Nanopore Sequencing Based Metagenomics Raises Concerns, *Int. J. Bio. Macromol*., 347, 150754 (2026). https://doi.org/10.1016/j.ijbiomac.2026.150754

Scharber, M. and Sariciftci, N., Low Band Gap Conjugated Semiconducting Polymers, *Adv. Mater. Technol.*, 6(4), 2000857 (2021). https://doi.org/10.1002/admt.202000857

Senff, L., João, A. L., Victor, M. F., Dachamir, H. and Wellington, L. R., Effect of Nanosilica on Rheology and Fresh Properties of Cement Pastes and Mortars, *Constr. Build. Mater.*, 23(7), 2487–2491(2009). https://doi.org/10.1016/j.conbuildmat.2009.02.005

Shafi, L. S., Megha, G. and Geeta, M., Comparative Study of Nanosilica Induced Mortar, Concrete and Self-Compacting Concrete – A Review, *Ind. J. Sci. Technol.*, 9(44), (2016). https://doi.org/10.1016/j.jclepro.2022.134116

Sorarù, G. D., Andrea, D. G., Campostrini, R., and Babonneau, F., Characterization of methyl-substituted silica gels with Si-H functionalities, *J. Mater. Chem.*, 5(9), 1363–1374 (1995). https://doi.org/10. 1039/JM9950501363

Vijayakumar, S., Chen, J., Amarnath, M., Tungare, K., Bhori, M., Divya, M., González-Sánchez, Z. I., Durán-Lara, E. F. and Baskaralingam, V., Cytotoxicity, phytotoxicity, and photocatalytic assessment of biopolymer cellulose-mediated silver nanoparticles, *Colloids Surf. A Physicochem. Eng. Aspects*, 628, 127270(2021). https://doi.org/10.1016/j.colsurfa.2021.127270

Rani, M., Keshu, Ankit and Shanker, U., Green Synthesis of a Biochar-Based Iron Oxide Catalyst for Efficient Degradation of Pesticides: Kinetics and Tran, T. K. N., van Tran, L. K., Thuyen Vo, N. C., Nguyen Vo, N. C., Doan, T. Q. M., Danh, H. D. and Nguyen, T. N. D., Green synthesis of titanium dioxide nanoparticles using green tea (*Camellia sinensis*) extract: Characteristics and applications, *Green Process. Syn.*, 14(1), 0226(2025). https://doi.org/10.1515/gps-2024-0226

Tan, Y., Li, Y. and Zhu, D. J., Preparation of silver nanocrystals in the presence of aniline, *Colloid Interface Sci.*, 258(2), 244-251 (2003). https://doi.org/10.1016/S0021-9797(02)00151-0

Tanimola, J. O. and Steve, E., Recent Advances in Nano Modified Concrete: Enhancing Durability, Strength, and Sustainability through Nanosilica (NS) and Nano Titanium (NT) Incorporation, *Appli. Eng. Sci.*, 19, 100189(2024). https://doi.org/10.1016/j.apples.2024.100189

Tsampali, E., Eirini, C. T., Eleni, P. and Maria, S., The Mechanism Action of Crystalline Admixtures on Hydration, Microstructure, and Self-Healing of Cementitious Materials, *J. Build. Eng.*, 110, 112987(2025). https://doi.org/10.1016/j.jobe.2025.112987

Wang, Y., Silveri, F., Bayazit, M. K., Ruan, Q., Li, Y., Xie, J., Catlow, C. R. A. and Tang, J., Bandgap engineering of organic semiconductors for highly efficient photocatalytic water splitting, *Adv. Energy Mater*., 8(24), 1801084 (2018). https://doi.org/10.1002/aenm.201801084

Wang, Z., Wang, X., Tu, L., Hao, W., Du, M., Dai, T., Guo, Q., Shi, Y. and Zhou, E., Dithienoquinoxalineimide-based polymer donor enables all-polymer solar cells over 19 % efficiency, *Angew. Chemie. Int. Ed.*, 63(21)/e202319755 (2024). https://doi.org/10.1002/anie.202319755

Wu, Q., Bhattacharya, M., Moore, L. M. J. and Morgan, S. E., Air processed P3HT: PCBM photovoltaic cells: morphology correlation to annealing degradation and recovery, *Wiley*, 52(23), 1511-1520 (2014). https://doi.org/10.1002/polb.23605

Yu, R., Tang, P., Spiesz, P. and Brouwers, H. J. H., A Study of Multiple Effects of Nanosilica and Hybrid Fibres on the Properties of Ultra-High-Performance Fibre Reinforced Concrete (UHPFRC) Incorporating Waste Bottom Ash (WBA), *Constr. Build. Mater.*, 60 98–110(2026). https://doi.org/10.1016/j.conbuildmat.2014.02.059

Zhan, P., Jing, X., Juan, W., Junqing, Z. and Zhihai, H., A Review of Recycled Aggregate Concrete Modified by Nanosilica and Graphene Oxide: Materials, Performances and Mechanism, *J. Clean. Prod.*, 375, 134116(2022). https://doi.org/ 10.1016/j.jclepro.2022.134116

Zhang, T., Qijun, Y., Jiangxiong, W. and Jianxin, L., Investigation on Mechanical Properties, Durability and Micro-Structural Development of Steel Slag Blended Cements, *J. Therm. Anal. Calorim.*, 110 (2), 633–639(2012). https://doi.org/10.1007/s10973-011-1853-6